Seismic-Response Assessment of Multiblock Tower Structures for Energy Storage: 1/25 Scale

Andres Rodriguez-Burneo, S.M.ASCE[1]; Jose I. Restrepo, Ph.D., M.ASCE[2]; Joel P. Conte, Ph.D., P.E., M.ASCE[3]; Jose E. Andrade, Ph.D., M.ASCE[4]; Ares Rosakis, Ph.D., M.ASCE[5]; Vahe Gabuchian, Ph.D.[6]; John Harmon, Ph.D.[7]; Arpit Nema, Ph.D.[8]; and Andrea Pedretti[9]

Abstract: This paper discusses the results of 1:25 scale shake table tests evaluating the seismic response of multiblock tower structures (MTSs) conceived as energy storage systems. The tests described here are a part of a comprehensive research campaign involving smaller physical models, computational model validation, and the theoretical background required to compare results across scales. The 6.46-m-high MTSs consisted of over 7,000 concrete blocks stacked vertically without any bonding agent, interacting only by friction and rocking. Three MTSs were tested under two different ground motions. Dynamic digital image correlation (DIC) and low-cost micro electrical mechanical system (MEMS) accelerometers were used for dynamic response measurements. Towers 1 and 3, subjected to repeated strong-intensity earthquake ground motions, collapsed during the third repetition due to the accumulation of residual displacements. Tower 2 was subjected to a single near-fault ground motion representing an extreme event and collapsed during the test. Different collapse mechanisms were identified in the test program. Data collected from individual blocks showed in-plane and out-of-phase block rotation and sliding, which contributed to the system's energy dissipation during the tests. **DOI: 10.1061/JSENDH.STENG-13144.**

Introduction

Technological advances in human civilizations have been marked by transformational developments in how energy is harvested, stored, and converted. From the invention of the potter's wheel in the southern Levant and northern Mesopotamia in the 5th and 4th millennium BC (Baldi and Roux 2016), respectively; the sailboat by the Egyptians in the 4th millennium BC (Quijada-Publins 2021); and water wheels in ancient China in the first millennium BC (Rao 2011) to the development of the Voltaic cell and flywheels in the 18th century (Piccolino 2000; Pennock 2007) and many other significant ways in the last 100 years, humanity has explored different ways to harvest, store, and transform energy. It is not difficult to forecast that progress will strongly depend on how current and future generations deal with energy, which, under the goals set out in the 1997 Kyoto international treaty, the 2015 Paris Agreement (UN 2021), and more recently, the Net Zero by 2050 White House Strategy (UNWH 2021), must be tied to climate action by adopting non-greenhouse gas–generating technologies. Because of the dire need to reduce greenhouse gases, the increase in energy demand nowadays is being met chiefly with wind and solar technologies. These two technologies have been growing at an unprecedented pace (BP 2022) and will continue to grow (EIA 2021). The main challenge with wind and solar technologies is their reliability because they are inherently intermittent, causing them to be often unavailable when required. Energy storage systems through chemical, electromechanical, thermal, magnetic, and mechanical technologies can be used to decouple energy supply and demand (McLarnon and Cairns 1989) and, for this reason, are becoming essential components in wind and solar energy generation technologies. Particular attention is being placed on the development of long-duration energy storage, where gravity-driven storage systems like multiblock tower structures (MTSs) could play a role (USDE 2023). MTSs are composed of compressed soil–cement blocks raised by an autonomous multiarm crane to store energy and dropped to generate energy when demanded; see Fig. 1. Each tower is designed to store up to 35 MWh. A MTS proof of concept was built by Energy Vault in Arbedo-Castione, Switzerland. Further details about the energy generation mechanism are described in Andrade et al. (2023).

This paper describes the results of a shake table test program on 1:25 scale MTSs. Three MTSs, comprising 38 levels each, were built and tested to collapse on the six-degrees-of-freedom (DOF) Pacific Earthquake Engineering Research (PEER)–UC Berkeley shake table located at the Richmond Field Station (in Richmond, California) of UC Berkeley and managed by the PEER Center.

[1]Graduate Student, Dept. of Structural Engineering, Univ. of California San Diego, 9500 Gilman Dr., La Jolla, CA 92093 (corresponding author). Email: a1rodrig@ucsd.edu

[2]Professor, Dept. of Structural Engineering, Univ. of California San Diego, 9500 Gilman Dr., La Jolla, CA 92093. Email: jrestrepo@ucsd.edu

[3]Professor, Dept. of Structural Engineering, Univ. of California San Diego, 9500 Gilman Dr., La Jolla, CA 92093. Email: jpconte@ucsd.edu

[4]Professor, Mechanical and Civil Engineering, California Institute of Technology, 1200 E California Blvd., Pasadena, CA 91125. Email: jandrade@caltech.edu

[5]Professor, Mechanical and Civil Engineering, California Institute of Technology, 1200 E California Blvd., Pasadena, CA 91125. Email: arosakis@caltech.edu

[6]Research Scientist, Graduate Aerospace Laboratories, California Institute of Technology, 1200 E California Blvd., Pasadena, CA 91125. Email: gabuchian@caltech.edu

[7]Graduate Student, Mechanical and Civil Engineering, California Institute of Technology, 1200 E California Blvd., Pasadena, CA 91125. Email: jhharmon@caltech.edu

[8]Postdoctoral Researcher, PEER, Univ. of California Berkeley, 1301 S. 46th St., Richmond, CA 94804-4698. Email: anema@berkeley.edu

[9]Chief Technology Officer, Energy Vault, Inc., 4360 Park Terrace Dr., Westlake Village, CA 91361. Email: andrea@energyvault.com

Note. This manuscript was submitted on August 28, 2023; approved on November 28, 2023; published online on March 6, 2024. Discussion period open until August 6, 2024; separate discussions must be submitted for individual papers. This paper is part of the ***Journal of Structural Engineering***, © ASCE, ISSN 0733-9445.

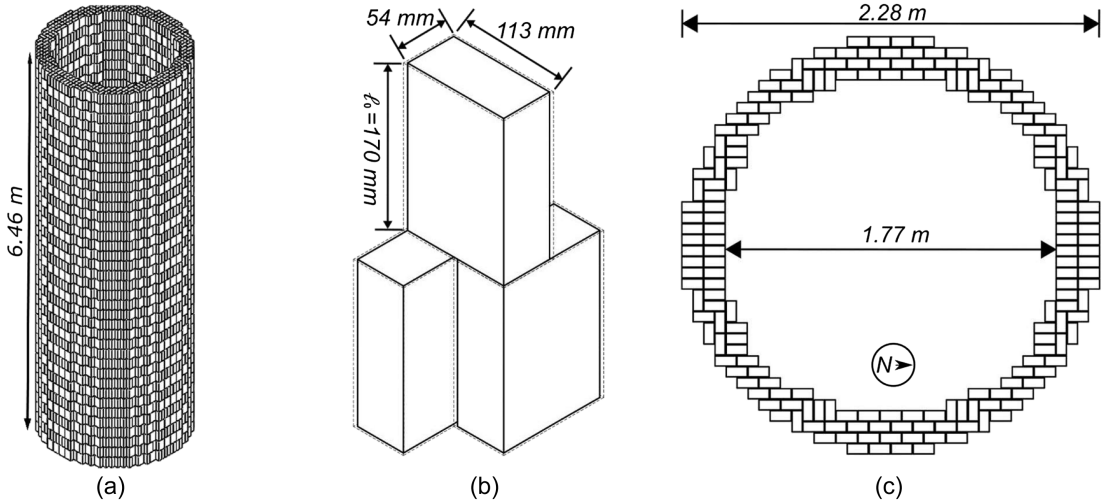

Fig. 1. Specimen description: (a) MTS model; (b) unit block and interlocking arrangement; and (c) block pattern in odd levels.

The testing described herein is a component of a major research effort conducted by a multiuniversity and industry team including the California Institute of Technology, the University of California at San Diego, the University of California at Berkeley, and Energy Vault. Key objectives of the comprehensive research campaign were to: (1) assess the structural response of such MTSs under earthquake-induced ground motions; (2) obtain experimental data for the validation of a discrete element computational model; and (3) develop dimensionless numbers and dynamic similitude laws relevant to the MTS, whose seismic dynamic response is governed by gravitational and frictional restoring forces acting on the discrete blocks that compose such structures. The reader is referred to the paper by Andrade et al. (2023) for detailed aspects of the overall research effort, Rosakis et al. (2021) for the development of the similitude laws and experiments at the 1:107 scale, and Harmon et al. (2023) for predictive modeling and simulation.

Test Program

Description of Scaling and Similitude

As described by Rosakis et al. (2021), MTS can be characterized as a discontinuous or discrete structure. These structures are composed of elements that are considered rigid, held together by gravitational and cohesive forces, in this case friction. In dynamic testing of structures, scaled experiments commonly rely on Froude or Cauchy scaling. Froude scaling is applied when gravitational forces govern the dynamic response, whereas Cauchy is used when elastic restoring forces are predominant and gravitational forces can be neglected (Harris and Sabnis 1999; Moncarz and Krawinkler 1981). Nonetheless, none of these scaling methods consider the effect of frictional forces. Rosakis et al. (2021) investigated a new set of dimensionless numbers that included frictional forces, referred to as μ-scaling, which was implemented in this research. The geometric scale was defined by the model's length l and was 1:25 of the prototype MTS; that is, $(l^M/l^P) = \lambda_l = (1/25)$, where superscripts M and P refer to the model and prototype, respectively. Model and prototype blocks were made of concrete, having the same density ρ and static friction coefficient μ. Thus, $(\rho^M/\rho^P) = \lambda_\rho = 1$ and $(\mu^M/\mu^P) = \lambda_\mu = 1$. Finally, because gravitational acceleration g could not be modified: $(g^M/g^P) = \lambda_g = 1$. Table 1 shows the μ-scaling laws required to satisfy similitude, along with a comparison to Froude scaling. In addition, the last column in Table 1 presents the model-to-prototype scale values obtained after applying μ-scaling with the constraints stated previously.

Specimen Description

The basic unit of the model MTS (hereafter termed tower) was a 54-mm-thick by 113-mm-wide by 170-mm-long concrete block manufactured in a commercial concrete paver press machine using a custom-made mold; see Fig. 1(b). The towers were composed of 38 levels (or layers) of blocks with the basic tiling pattern shown in Fig. 1(b). Each level consisted of 188 blocks. Odd levels were arranged as depicted in Fig. 1(c), whereas even levels were built by rotating this pattern 90°. This ensured that every block remained in contact with two other blocks underneath in a simple interlocking pattern.

Table 1. Scaling laws and scaling factor

Physical quantity	Froude-scaling dimensionless Number Π	μ-scaling dimensionless Number Π	μ-scaling law	Model to prototype ratio
Velocity (v)	$\frac{v}{\sqrt{l\,g}}$	$\frac{v}{\sqrt{l\,\mu g}}$	$v^M = v^P\sqrt{\lambda_l\lambda_g\lambda_\mu}$	$\frac{v^M}{v^P} = \frac{1}{5}$
Acceleration (a)	$\frac{a}{g}$	$\frac{a}{\mu g}$	$a^M = a^P\lambda_\mu\lambda_g$	$\frac{a^M}{a^P} = 1$
Time (t)	$t\frac{1}{\sqrt{l}}$	$t\sqrt{\frac{\mu g}{l}}$	$t^M = t^P\frac{\sqrt{\lambda_l}}{\sqrt{\lambda_\mu\lambda_g}}$	$\frac{t^M}{t^P} = \frac{1}{5}$

J. Struct. Eng., 2024, 150(5): 04024040

Table 2. Concrete block properties

Property	Min	Max	Avg.
Concrete density (kg/m^3)	2,245	2,412	2,376
Concrete compressive strength (MPa)	27.2	64.3	43.1
Modulus of elasticity (GPa)	29.4	39.4	34.4
Static friction coefficient–block on block	0.44	0.53	0.50

Concrete Block Characterization

The physical properties of the blocks required for this study included the modulus of elasticity, compressive strength, and static friction coefficient. Values measured from a sample of five blocks are presented in Table 2. The static friction coefficient was obtained using a tilting surface and measuring the critical angle at which block-on-block sliding initiated.

The model blocks were built to tight dimensional specifications to guarantee adequate specimen construction. Small fabrication tolerances were specified to obtain the specified dimensions. The towers were tested with blocks that were no more than 2 weeks of age to avoid significant volumetric changes. Because the blocks on a given level were not in contact with each other, the most critical dimension was the block height. As a first quality check, each block was passed through a test stencil to eliminate those whose dimensions were significantly larger than specified. This resulted in the rejection of about 20% of the blocks manufactured for this research project. The second quality check was to match the blocks' height per level. To determine the variability of the height of the blocks that passed, a sample of 50 blocks were surveyed. The height measurement revealed that the variability was characterized by three discrete values based on the molds used for fabrication. These blocks were either 169.07, 169.86, or 170.66 mm high. The measured blocks' height variations were incorporated into a discrete-element model of the tower (Harmon et al. 2023).

Interface Characterization: Base-to-Block Friction Coefficient

The experiment required the same coefficient of friction between the base of the tower and the shake table steel platen and in between blocks. Polymer jointing sand was placed on top of the table, wetted, and left to dry to provide the desired base-to-block coefficient of friction. A close-up of this interface can be observed in Fig. 2. Tests were carried out to ensure that the sand-to-concrete coefficient of friction was as close as possible to the block-to-block value specified in Table 2. The static friction coefficient was obtained using a tilting table to measure the angle at which sliding first occurred, as described in Harmon et al. (2023). A value of 0.53 was found for the sand-to-block friction coefficient, which is very similar to the average static friction coefficient obtained for the block-to-block friction. The entire scaled system, including tower and base, can be characterized with a single static friction coefficient. Setting this layer (see Fig. 2) was the important first step of specimen construction, described in the following section.

Specimen Construction

Specimen construction played a major role in the experimental campaign. It required the careful design of a system that would allow the safe stacking of over 7,000 blocks to a total height exceeding 6 m. Moreover, this construction support system had to be disassembled before each test without compromising the structural integrity of the tower.

Construction of the specimen followed a procedure where a template (or stencil) was used to build one level (or layer) of the tower at a time. A similar approach was used on the models built at a 1:107 scale at the California Institute of Technology (Rosakis et al. 2021). However, for this experiment, the system incorporated a central guide tube and four stays, whose design was inspired by the Paplanta flyer dancers (Schoneich 2014); see Fig. 3(a). The steel stencil was designed and computer numerical control (CNC)-cut from a 25-mm-thick steel plate to build the block pattern of each level shown in Fig. 1(c). Given the size of the stencil, it had to be CNC-cut in two separate pieces, which were welded afterwards. Fabrication of the stencil required a tolerance not exceeding 0.8 mm to guarantee the quality of the final tower. A photo of the stencil is shown in Fig. 3(b).

A crane system, shown in Fig. 3(a), was designed to lift and rotate the stencil without compromising the blocks already placed and to ensure safety. The elements of this system included a seamless round central column (guide pole), 4-four cantilevered beams resting on top of the column (top cross), 4-four threaded steel rods (stays), and two outer square columns. The stays were used to hang the stencil from the beams at the top. The stays consisted of 1″-diameter, 1-8″ Unified National Coarse Thread (UNC) threaded bars. The stencil rested on hexagonal nuts placed at the proper height along the bars, as seen in Fig. 3(b). The coarse thread with a pitch of 25 mm allowed one to lift the stencil steadily by rotating the nuts together. The outer columns had the purpose of keeping the stencil in position while placing the blocks. After completing a level, the stencil was lifted by manually turning the nuts underneath. This

Fig. 2. Tower base to shake table platen interface: (a) close-up of sand base and first two levels; and (b) close-up of base-to-block interface.

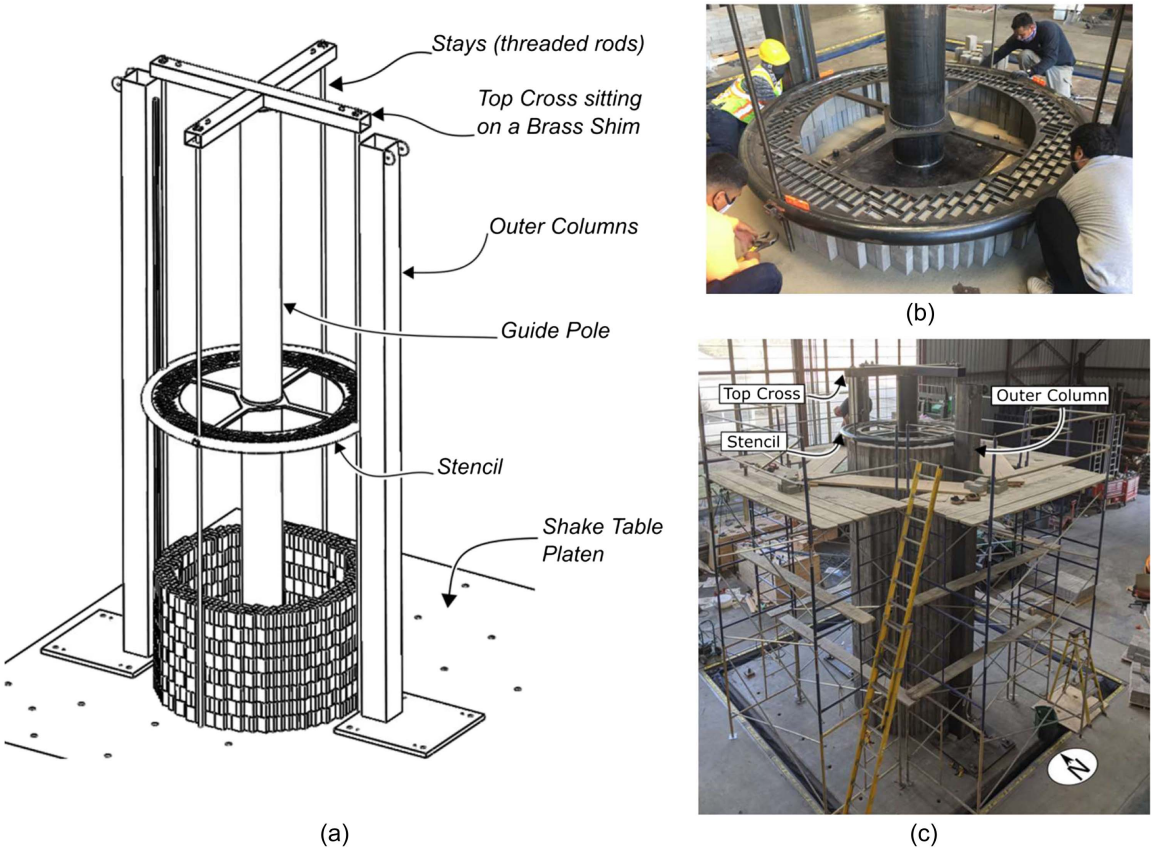

Fig. 3. Specimen construction: (a) crane system concept; (b) lifting of stencil; and (c) construction process at the 30th level.

mechanism allowed the stencil to rise evenly from all sides without displacing the blocks that had been placed.

Once the base had been prepared, with polymer jointing sand (see the "Interface Characterization: Base-to-Block Friction Coefficient" section) the guide pole and outer columns were bolted to the top of the table. Additional leveling bolts on the base plates were used to keep the columns plumb. Column verticality was checked and corrected during several stages of the construction process. Subsequently, the stencil was inserted into the guide pole and lowered. Finally, the top cross was placed on top of the central column, resting on a greased brass disk that allowed the smooth rotation of the cross. The stays were then inserted in position, secured at the top cross, and used to hang the stencil.

With the tower assembly system in place, the construction sequence proceeded as follows: first, the stencil was leveled and secured using the outer columns; then, the 188 blocks of the current level were placed, as shown in Fig. 3(b). Afterward, the stencil was lifted to disengage the placed blocks by turning the nuts underneath and rotated 90° by rotating the top cross along with the stays. Finally, the stencil was once again restrained at the proper position to proceed with the next level. This procedure was repeated until the 38 levels were completed. As the number of built levels increased, scaffolding was required to continue with the construction process. Fig. 3(c) shows a photo of the construction of the tower at the 30th level.

Given the dimensions of the construction system, a structural analysis was performed of all the elements of the crane system. This was to verify the strength of the elements and control deflections that could have affected the quality of the final product, the built tower.

The design of the crane system also considered the disassembly procedure. Upon completion of the tower, all the elements except for the guide pole had to be removed following a specific sequence. This procedure ensured that the specimen would not be compromised after its construction was completed. Fig. 4(a) shows the completed tower after removing all the elements used for its construction.

Despite the quality control of the blocks and the measures taken during the design and assembly of the tower construction system, there was a clear misalignment between blocks. Figs. 4(b and c) show a close-up of the completed tower where imperfections can be observed. These imperfections included slightly tilted blocks and consecutive levels not perfectly aligned. The imperfections can be attributed to the height variability of the blocks, human error during construction, and alignment of the stencil.

Specimen construction was a challenging multiday procedure that could not be overlooked during the research campaign. It required a construction crew to sort the blocks, build the specimen, and assemble and disassemble the crane system and scaffolding. The three towers were built and tested during a lapse of 30 days in October–November 2020. Supplemental Video S1 shows a time-lapse of the construction process of Towers 1 and 2.

Earthquake Input Ground Motions

Two earthquake input ground motions were used throughout the campaign. The first ground motion was recorded at the China Lake station during the July 6, 2019, M_w 7.1 Ridgecrest Earthquake. The Ridgecrest Earthquake was selected because it represents a

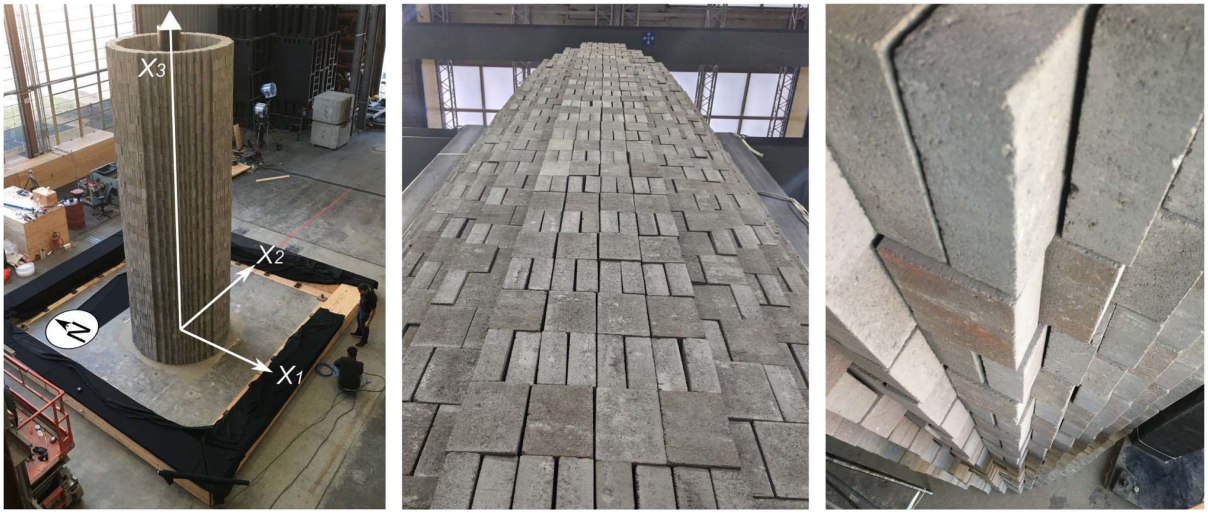

Fig. 4. Tower 1 as constructed: (a) overall view and definition of axes; (b) close-up from the bottom and showing defects; and (c) close-up from the top showing defects.

cross-fault rupture common to southern California (Barnhart et al. 2019), which was a potential location for the MTS.

The second earthquake input ground motion was recorded 3 km away from the fault at Pump Station 10 (PS10) by the Alyeska Pipeline Service Company during the November 3, 2002, M_w 7.9 Denali Earthquake. This second ground motion was characterized by a single one-sided pulse due to "supershear" stress release (Dunham and Archuleta 2004).

Towers 1 and 2 were subjected to the three-component Ridgecrest and Denali ground motions, respectively. Tower 3 was subjected to only the strong-motion (fault-parallel, north–south direction) component of the Ridgecrest ground motion. This tower was tested to recreate the same experiment conducted at the 1:107 scale MTS (Rosakis et al. 2021) and validate the scaling procedure used for the specimens and the ground motion records. In the results section, the seismic input records are referred to as Ridgecrest 3-D, Denali 3-D, and Ridgecrest 1-D. Information regarding each of the earthquake ground motions used is summarized in Table 3.

Table 3. Test setup summary

Tower	Ground motion	Components	Accelerometers	DIC
1	Ridgecrest 3-D, 1	x_1, x_2, x_3	No	Yes
	Ridgecrest 3-D, 2		No	Yes
	Ridgecrest 3-D, 3		No	Yes
2	Denali 3-D	x_1, x_2, x_3	Yes	Yes
3	Ridgecrest 1-D, 1	x_1	Yes	Yes
	Ridgecrest 1-D, 2		Yes	No
	Ridgecrest 1-D, 3		Yes	Yes

Test Setup

Fig. 4(a) shows the location of the tower on the shake table as well as the adopted coordinate system. Lights and cameras for dynamic digital image correlation (DIC) data collection were located on the east side or front of the tower. Accelerometers were placed on the west side or back of the tower. Further details of the instrumentation are explained in the following section.

Regarding the direction of the input ground motion, for the three-component seismic experiments, the strong motion (fault parallel component) was applied in the north–south direction, referred to as the x_1 axis; see Fig. 4(a). Similarly, this is the direction in which the input ground motion was applied for the single-component seismic test. Accelerometers and cameras for DIC were used to measure and record the dynamic response of the tower. Some experiments used both instrumentation systems, whereas others relied on accelerometers or DIC cameras only. The instrumentation used for each test is provided in Table 3.

Fig. 4(a) shows the specimen after the construction system had been disassembled. However, it was observed that the central column could not be removed after construction and was left in place during all tests. It should be mentioned that the shake table was calibrated with the central "guide pole" attached to it to account for its weight and dynamic response when reproducing the earthquake input ground motions.

Instrumentation

Dynamic Digital Image Correlation

Two high-speed cameras were collectively triggered prior to the start of the shake table motion by a TTL signal sent from the shake table controller. Camera A consisted of a Phantom v2640 (Vision Research, Wayne, New Jersey) (Phantom 2023) with a 2,048 × 1,952 high-resolution sensor operating at 2,000 fps, and Camera B consisted of a Phantom v300 (Vision Research, Wayne, New Jersey) with a 1,080 × 700 sensor set to operate at 1,400 fps. Each camera captured progressive frames with no field interlacing. Four high-latency Arri T12 12kW tungsten filament lights uniformly illuminated the front of the tower for Camera A, and two Arri 2 kW tungsten open face lights (Arri Group, Burbank, California) (ARRI 2023) illuminated the top of the tower for Camera B. Camera exposure times ranged from 200 to 300 μs to prevent motion blur within captured frames. The combination of camera sensor resolution, exposure time settings, light selection, and frame composition are all required ingredients for successful motion tracking. This optical setup was scaled up from the initial tests conducted at 1:107 scale.

The goal of the setup shown in Fig. 5(a) was to achieve photographs of the tower such that the viewer would not be able to distinguish the true size of the tower. Such a strategy made it

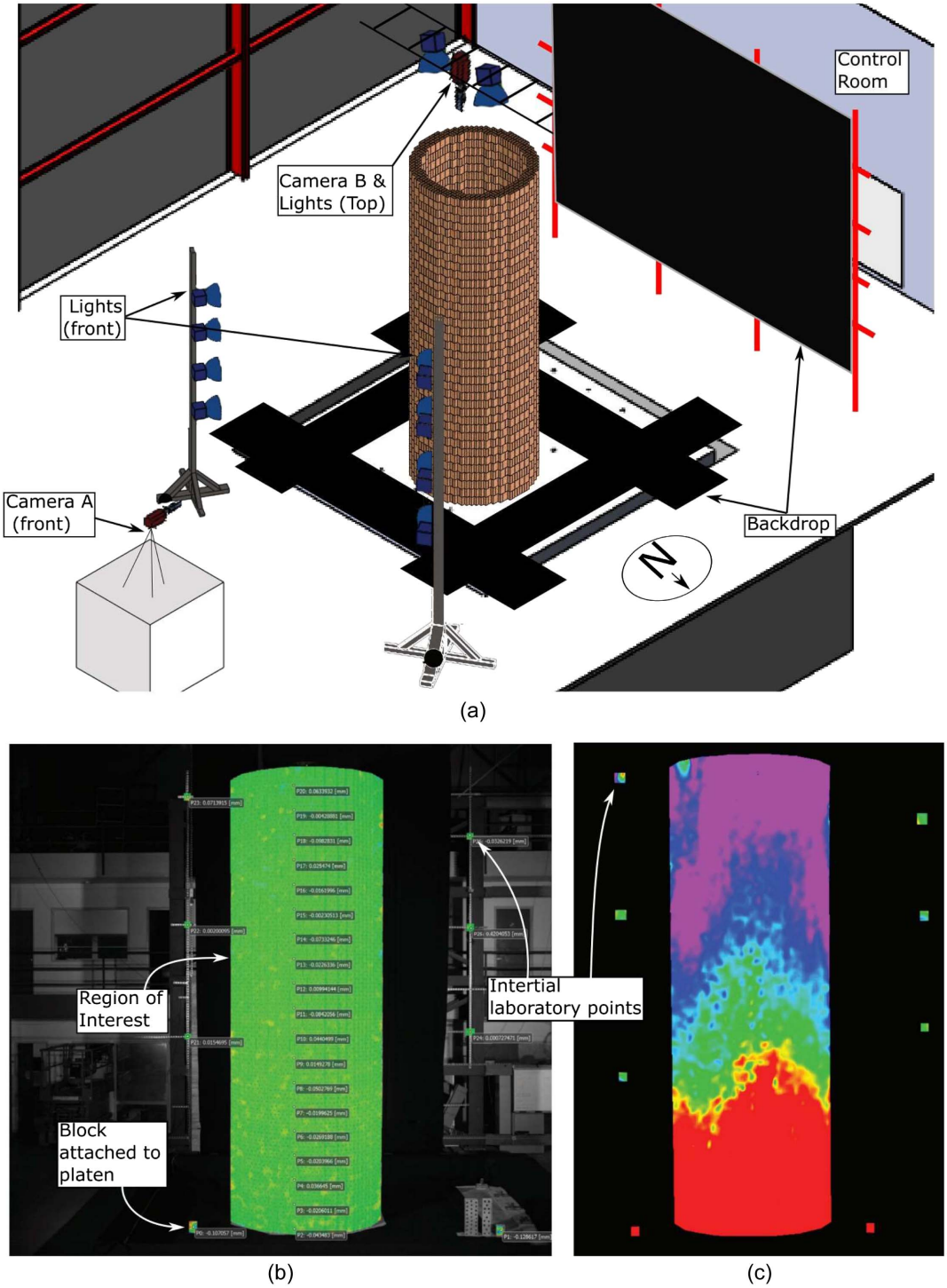

Fig. 5. Instrumentation for DIC: (a) optical setup observing front and top of tower; (b) raw image from Camera A with region-of-interest; and (c) processed image of velocity field with inertial points.

impossible to distinguish the towers built at 1:25 scale (this paper) and at 1:107 scale (Rosakis et al. 2021). By keeping the object–observer perspectives locked across scales, and indeed in virtual simulations (Harmon et al. 2023), one can process the images in a similar fashion and can directly compare measurement and predictive modeling results. The output from the cameras displayed in Figs. 5(b and c) is further described in the "Results" section.

A challenge to this optical measurement technique when used under dynamic conditions was to avoid table-induced vibrations that would excite the cameras. For this reason, it was important to have an inertial reference frame as the observer (cameras) to ensure that the recorded motions were indeed of the object (specimen) rather than a convolution of the camera and specimen motions. One way to achieve this was to set the observers far away from the test or to have inertial markers in the camera frame that could

compensate for camera motions. Because maximizing the use of the camera sensors (increasing the px/mm ratio) was prioritized during these tests, the camera proximity to the tower was set, and it was accepted that camera motions would occur. To remove the camera motion, several inertial points along the shake table facility building structure were tracked; a set of points on both sides of the tower can be observed in Fig. 5(b). A three-point triangulation was used to correct both camera rotation and translation with respect to the inertial points. Removal of the camera rigid body motion immediately revealed the displacement field obtained from the tower. Usage of DIC was successfully implemented in structural testing.

Accelerometers

An array of 19 low-cost 3-g triaxial analog accelerometers was installed on a few concrete blocks at discrete locations along the back side of the tower. The accelerometers had an operational bandwidth from DC to 550 Hz, and measurement data were recorded at 2,000 samples per second (Adafruit 2021) to match the Camera A frame rate. These accelerometers were chosen due to their small size and as sacrificial sensors due to the high likelihood of being damaged during a collapse of the specimen.

Fig. 6(a) shows the back side of the tower where shaded blocks indicate the locations of the accelerometers. The levels marked in the figure were selected based on the observed dynamic response of the 1:107 scale tower specimen tested at Caltech (Rosakis et al. 2021).

In addition, as seen in Fig. 6(a), some accelerometers were placed on both sides of the plane of symmetry of the tower, referred to as the spine. The labels "left-spine" and "right-spine" are used to identify data presented in the "Results" section. Two accelerometers were placed on each of the selected blocks [see Fig. 6(b)] to obtain the six-DOF movement of the instrumented blocks, including roll, yaw, interblock rotations, and slip. Unlike DIC data, which provided measurement data over the entire front face of the tower, the accelerometers only measured the tower's response along the spine on the back side. This arrangement of accelerometers was only used in Towers 2 and 3; see Table 3.

Finally, six single-axis accelerometers from Measurement Specialties es (TEC 2023) were placed in two three-axis configurations on top of the shake table platen. The two sets were installed at the table's southwest and northeast corners to measure the input ground motion and compare it with the table acceleration feedback signal provided by the shake table controller.

Test Results

This section discusses the seismic response of the MTS by examining the behavior of the blocks at different levels of the tower with measurements obtained from DIC (on the front face) and accelerometers (on the back face). The observed failure mechanisms were analyzed for all three towers. However, the analysis of results is emphasized for Tower 3 because this tower was the most heavily instrumented and was subjected to three runs of the Ridgecrest 1-D ground motion.

Data captured with DIC enabled the assessment over the entire front face of the towers (see Fig. 7) whereas accelerometers allowed the evaluation of the response only at the blocks located next to the spine of the towers. Fig. 7(a) shows the horizontal particle velocity map (v_1) for the entire face of Tower 1 at a sequence of times during all runs of the Ridgecrest 3-D input ground motion. Seismic waves can be seen propagating from the base to the top of the tower. Time series were extracted and plotted in Fig. 7(b) from the points marked by the black dots along the spine of the tower. Supplemental Video S2 contains the complete time-history of the snapshots depicted in Fig. 7(a).

All towers were tested until collapse; see Fig. 8. Towers 1 and 3, subjected to Ridgecrest 3-D and 1-D, respectively, were able to withstand the input ground motion twice before collapsing during the third repetition of the test. Tower 2, on the other hand, collapsed during the first and only execution of the PS10 record of the Denali

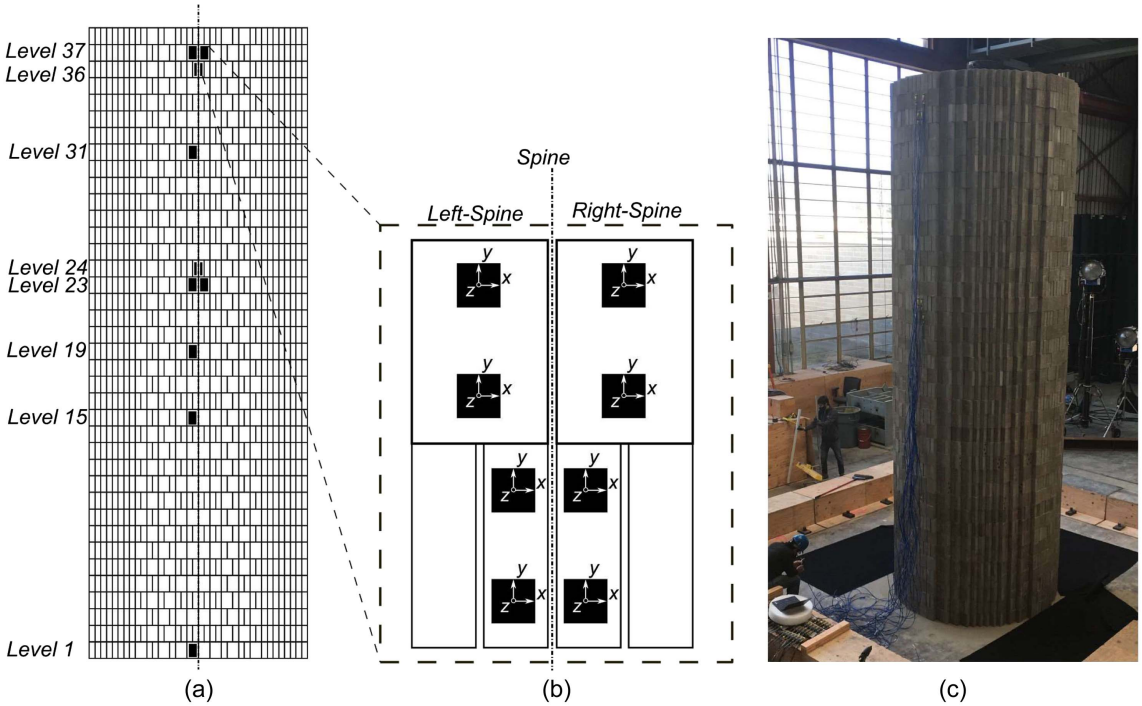

Fig. 6. Accelerometer instrumentation: (a) general layout; (b) array of accelerometers per block; and (c) instrumentation on back side of Tower 3.

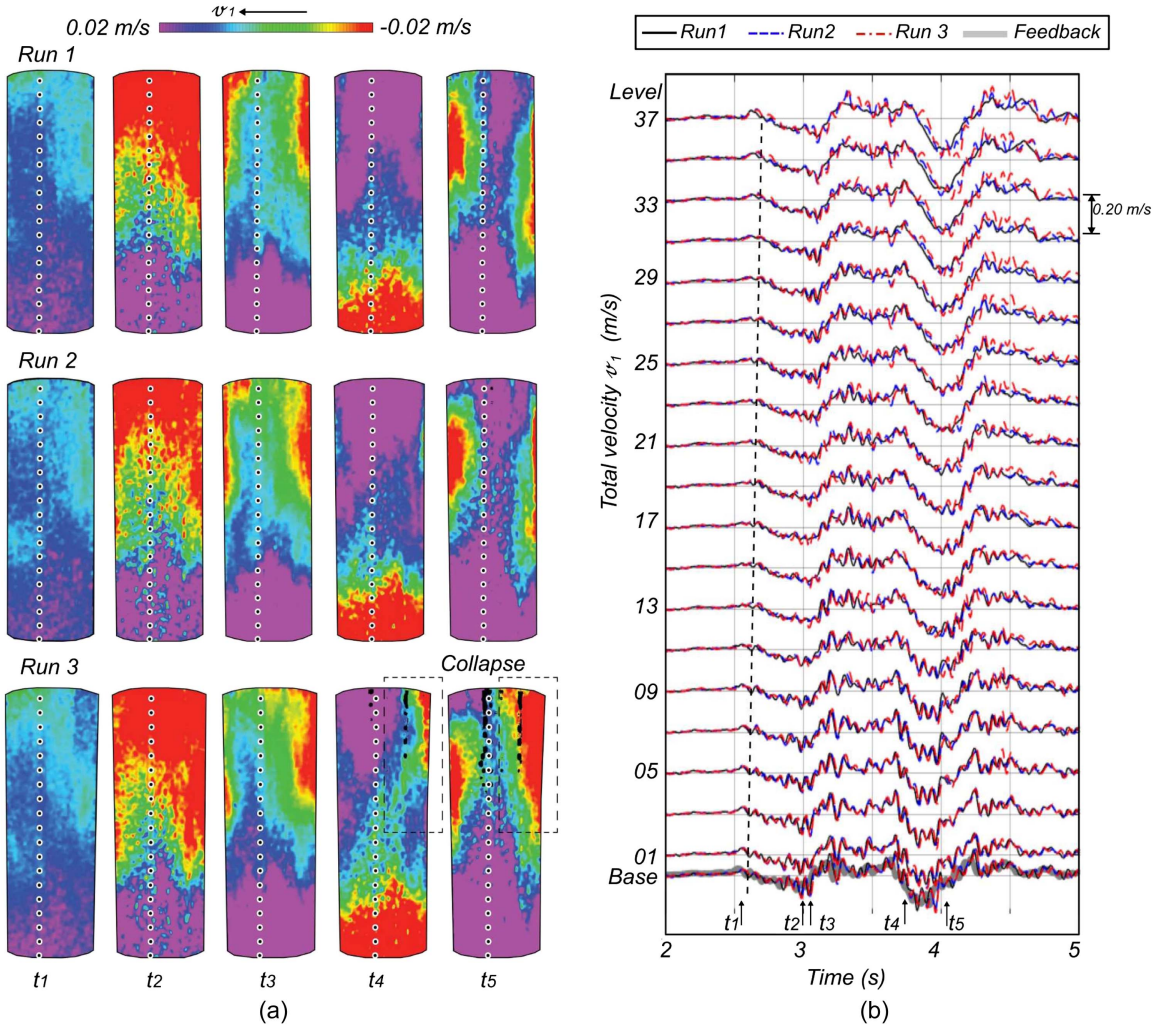

Fig. 7. Tower 1 total particle horizontal velocity map (v_1) from the sequence of Ridgecrest 3-D input x_1: (a) v_1 at times t_1–t_5 for runs 1–3; and (b) v_1 time series from the dots distributed along the spine of the tower.

Earthquake. Snapshots of the onset of the collapse of Towers 2 and 3 are shown in Fig. 8. The full collapse of Towers 2 and 3 can be found in Supplemental Videos S3 and S4, respectively. To further investigate the response at this stage, accelerometer results were analyzed. Fig. 9 shows the time histories of the total acceleration a_1 of Tower 2 and Tower 3-Run 3 in the x_1 direction. The black dots represent the instant of time at which data from two adjacent blocks began to diverge, indicating significant rotations that modified the orientation of the accelerometers; thus the onset of the collapse. Tower 1 was not instrumented with accelerometers. Therefore, only Towers 2 and 3 are shown in Fig. 9.

Figs. 10(a–c) depict the left-spine block total velocity response time histories in the v_1-direction, v_2-direction, and v_3-direction, recorded for Tower 2, tested under the 3-D Denali input ground motion, and Fig. 10(d) shows the block total velocity response time-history v_1 in the x_1-direction recorded for Tower 3-Run 1, subjected to the 1-D Ridgecrest input ground motion.

Rosakis et al. (2021) defined structural speed as the velocity at which motion propagates through the tower's height. It can be computed by dividing the distance between two levels by the time delay of the arrival of the seismic wave. Arrival of the wave at the base was identified by locating the onset of sliding. The onset of sliding was defined as the instant where the total velocity response above the base of the tower differed from the total velocity at the base. Subsequently, to objectively determine the time delay, the cross-correlation function between the velocity records at the base and at the level of interest, the top level in this case, was computed, and the time lag at the maximum value of the cross-correlation function was taken as the time delay. Only one second of the response (or 2,000 data points) before and after the onset of sliding was used for the computation of the cross-correlation function to make sure that only the propagation of the first wave was considered. In Fig. 10, the solid line connects the points of the onset of sliding at the base and the arrival of the corresponding wave at the top, with these two points separated by the time delay. This helps visualize how the wave propagates along the height of the tower. Graphically, the slope of the line corresponds to the structural speed between the two specified levels. The propagation of the wave obtained via DIC is also shown in Fig. 7(b) for Tower 1. Table 4 summarizes the structural speed results using DIC and the accelerometers for each tower.

Furthermore, Figs. 11 and 12 show the response time-history results obtained using both DIC and the low-cost accelerometers for Tower 3-Run 1 and Tower 2, respectively. These figures present the total and relative velocity and displacement responses, respectively. The labels "left-spine" and "right-spine" refer to which side

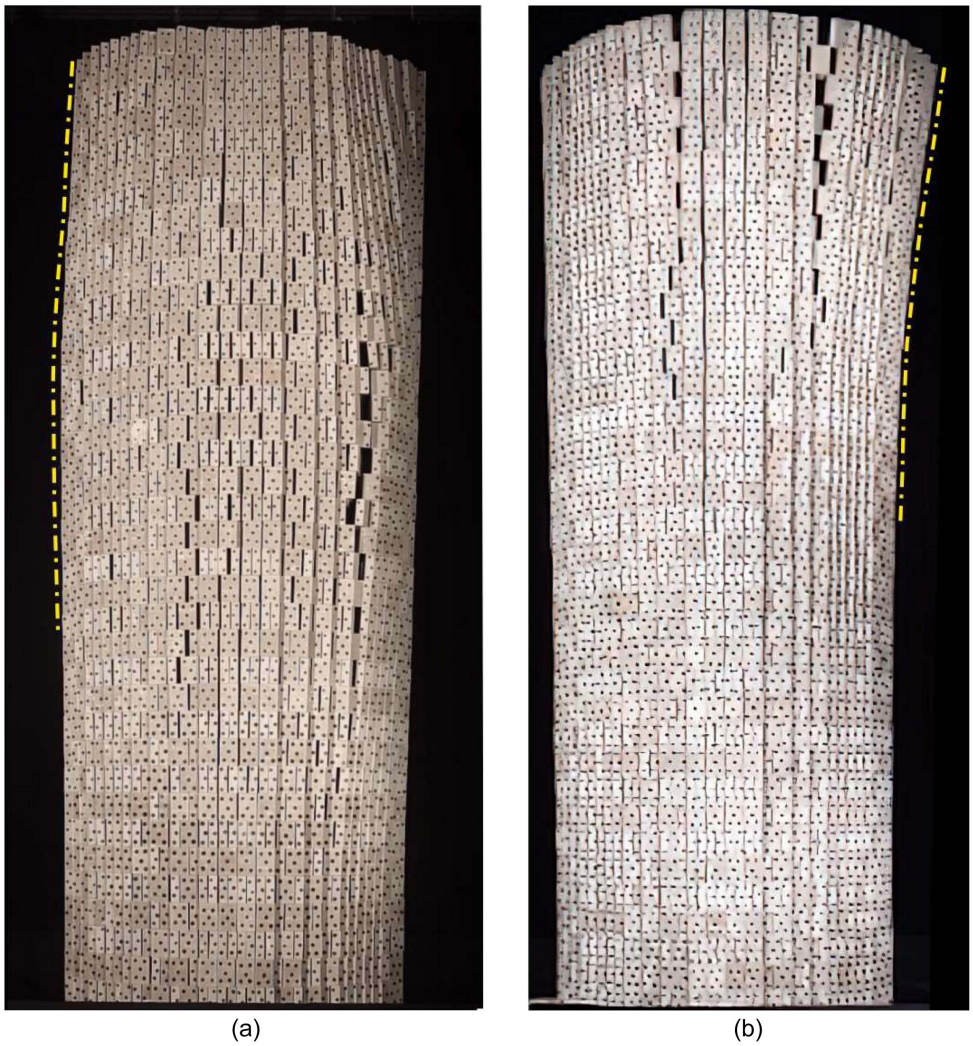

Fig. 8. The onset of collapse: (a) buckling mode from Tower 2, Denali 3-D; and (b) peeling mode from Tower 3, Ridgecrest 1-D.

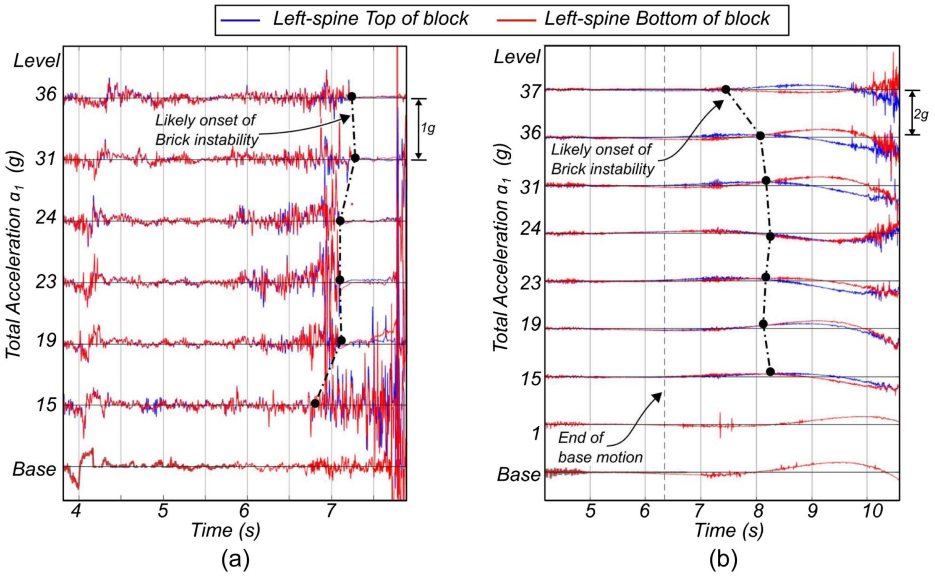

Fig. 9. Identification of onset of collapse: (a) Tower 2, x_1 total acceleration a_1; and (b) Tower 3, Run 3, total acceleration a_1. Left-spine, right-spine.

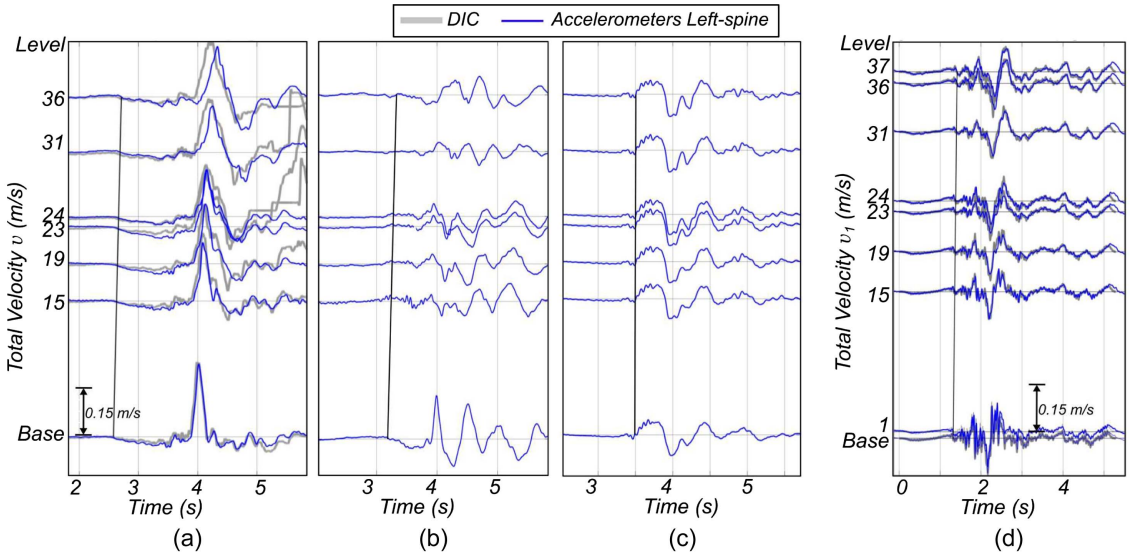

Fig. 10. Left-spine block total velocity response showing the structural speed (wave propagation along the tower's height): (a) Denali v_1; (b) Denali v_2; (c) Denali v_3; and (d) Ridgecrest 1-D v_1.

Table 4. Structural speed results

			Structural speed (m/s)	
Ground motion	Direction	Run	Via DIC	Via accelerometers
Ridgecrest 3D	x_1	1	86	—
Ridgecrest 3D	x_1	2	62	—
Ridgecrest 3D	x_1	3	56	—
Denali 3D	x_1	1	55	47
Ridgecrest 1D	x_1	1	78	81
Ridgecrest 1D	x_1	2	—	70
Ridgecrest 1D	x_1	3	72	62

of the spine the block is located, as shown in Fig. 6(b). Further details on the data processing and comparison of results are discussed in the following sections.

Achieved versus Target Input Ground Motion

For each of the three tower specimens, the earthquake input motions to be reproduced by the UC Berkeley shake table (UCB 2023) were obtained by scaling the two actual earthquake ground motions considered in this study and defined previously (2019 M_w 7.1 Ridgecrest Earthquake and 2002 M_w 7.9 Denali Earthquake) using the μ-scaling law (see Table 1). The shake table controller (MTS 4690D) was then tuned with only the center "guide pole" on the table (to avoid perturbing the tower specimens before testing) for each of the target (desired) earthquake input motions. The tuning involved setting optimum values of the feedforward and feedback gains in the control loop as well as the application of an iterative time history matching technique (repeatedly modifying the command input or drive file to the shake table controller) to optimize the tracking of the target earthquake input motion by the table (i.e., minimize the discrepancy between the target earthquake input and the achieved shake table motion).

The shake table controller also applied a band-pass filter to the μ-scaled earthquake input motions. As a representative example, Fig. 13(a) compares the target input motion (in terms of acceleration, velocity, and displacement in the x_1-direction) with the achieved table motion (1) measured using accelerometers installed on the edge of the table and (2) obtained from the shake table controller through signal processing applied to the feedback table displacement and acceleration measured through the actuator linear variable differential transformers (LVDTs) and control feedback accelerometers for the case of Tower 1 subjected to the Ridgecrest 3-D input motion, first run. The acceleration measured using the accelerometers installed on top the table was band-pass filtered between 0.2 and 200 Hz and double integrated in the frequency domain (Fourier integrated) to obtain the table velocity and displacement. It was observed that: (1) the measurements of the achieved motion obtained from the accelerometers installed on top of the table and from the shake table controller were relatively close, and (2) the discrepancy between the target earthquake input motion and the achieved table motion was reasonable. This discrepancy was due to the imperfect nature of the shake table controller (acting on a complex nonlinear dynamic system such as the UC Berkeley shake table) and the dynamic interaction between the tower and the shake table.

Good agreement between the target and achieved ground motion was also observed in the response spectra. Figs. 13(b and c) show the acceleration and displacement, 5% damping, response spectra of the input ground motions used for Towers 1 and 2 in the x_1-direction. The concept of elasticity was not as relevant when assessing response of the MTS. The towers are discontinuous and discrete structures whose dynamic response was governed by friction and rocking rather than elasticity. For this same reason, neither the mode shapes nor the natural periods were relevant in the description of the seismic response. Nonetheless, the response spectra are still included to provide a better grasp of the intensity of the ground motions used in the research campaign.

Particle Displacement Response Measured Using Dynamic DIC

The data frames extracted from each camera's raw video output were properly processed, generating a sequence of images; see Fig. 5(b). The first frame at time t_0 captured the tower in its as-constructed configuration by design because the cameras were ensured to trigger prior to any motion of the shake table. Fig. 5(c) shows the tower in its updated configuration at time t_1, and so on until the final frame of the sequence at time t_f.

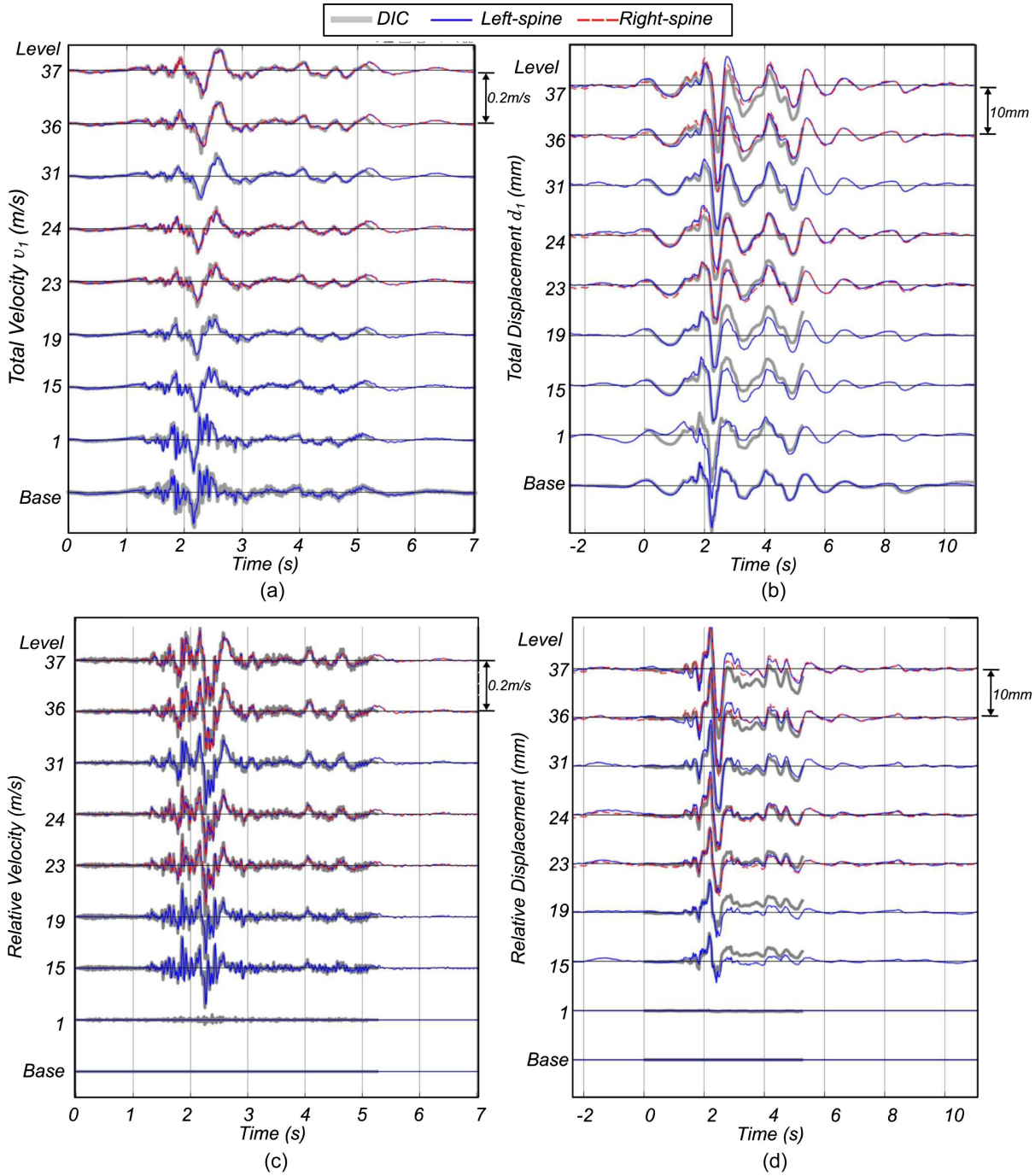

Fig. 11. Block response time history for Tower 3 subjected to Ridgecrest 1-D, Run 1: (a) total velocity v_1; (b) total displacement d_1; (c) relative velocity; and (d) relative displacement in x_1 direction.

Motion tracking was achieved with Correlated Solutions VIC-2D (Correlated Solutions 2022) by tracking grayscale value signatures across the entire image sequence representing the full video capture. VIC-2D analyzes the grayscale values in the reference image (at time t_0), where displacements are set to 0 by definition, then updates the change in position of each unique subset frame by frame. The output of the analysis yields the time evolution of the displacement field within the predefined region of interest. Once the displacement field is properly obtained, extractions of points and calculation of the velocity and accelerations filed follow via standard numerical derivation techniques.

Response Measurements from Accelerometers

All velocity and displacement response time histories were obtained by integrating the corresponding acceleration response in the frequency domain. The recorded acceleration response data had to be processed before integration. Signal processing details, along with the limitations encountered on it, are described in the following. Acknowledging the limitations of the methods used for signal processing allowed us to better interpret the velocity and displacement results.

For the signal processing procedure, a fifth-order Butterworth bandpass filter with corner frequencies at 0.2 and 100 Hz was

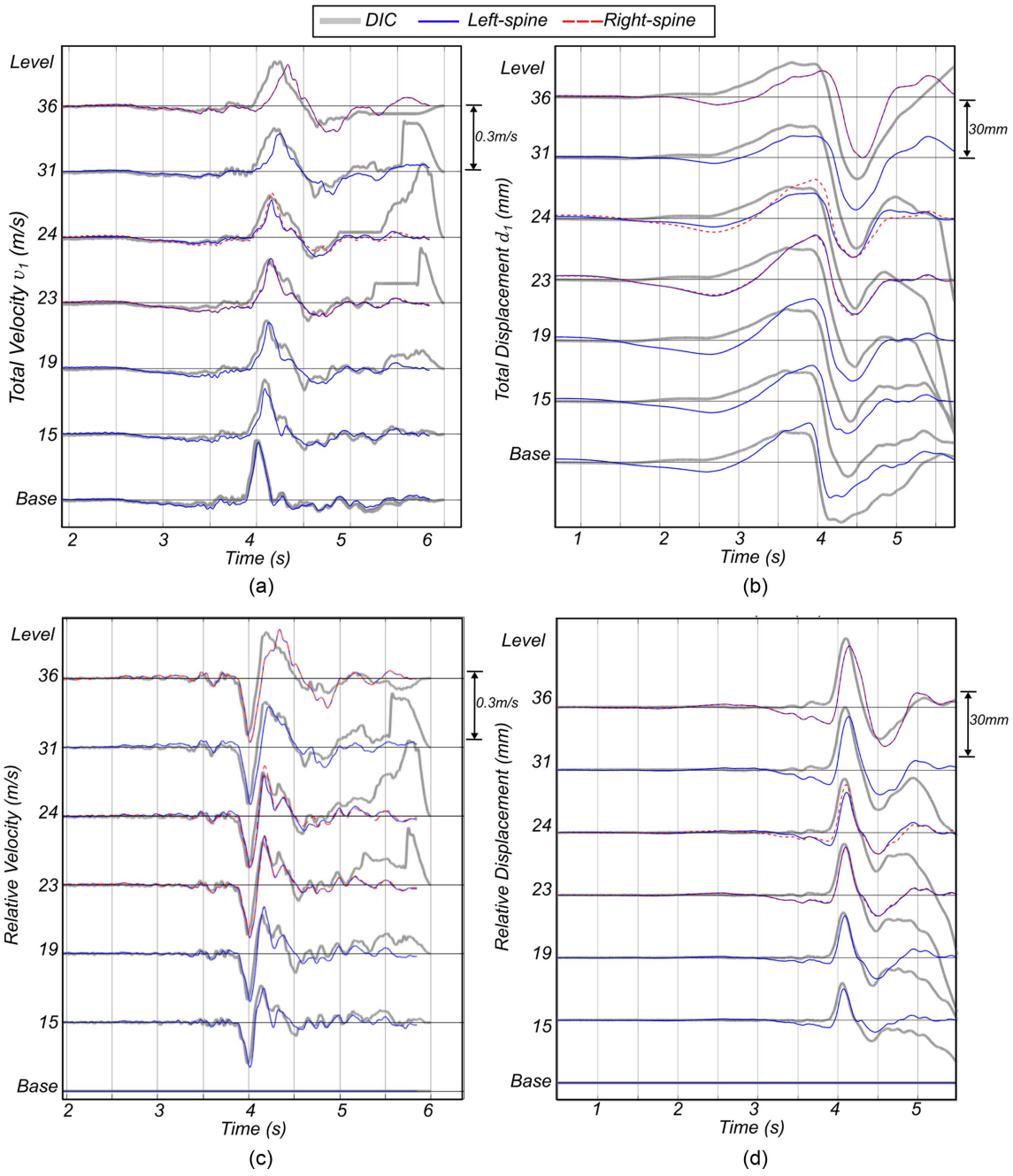

Fig. 12. Block response time history for Tower 2 subjected to Denali 3-D: (a) total velocity v_1; (b) total displacement d_1; (c) relative velocity; and (d) relative displacement in x_1 direction.

applied to the acceleration records. Additionally, a high-pass filter at 0.3 Hz was applied to the velocity records prior to integrating them into displacements. The corner frequencies were carefully selected after evaluating the frequency content of the raw data in the Fourier spectra. The DIC velocity results were obtained through numerical differentiation of the measured displacement results. Results obtained using both accelerometers and DIC are shown in Figs. 11 and 12. Despite the good agreement between the DIC and accelerometer-based results, it can be observed that there was no perfect fit between both instrumentation systems. A perfect fit was not expected to occur because DIC measured the response of the front face of the tower, whereas the accelerometers measured the response of the opposite side. This difference was more pronounced on Tower 2 because it was subjected to the Denali 3-D seismic input, whose additional components introduced more discrepancies between the response at the front and back of the tower, especially at higher levels; see Fig. 12. These differences also influenced the structural speed (see Table 4). A DIC and accelerometer comparison shows that structural speed obtained for Tower 3, which was subjected to 1-D input motion, was much closer than that for Tower 2, which was subjected to a 3-D input motion. Nonetheless, the somewhat surprising agreement between the DIC and accelerometer-based measured response provides confidence that the data filtering procedure was appropriate.

Moreover, a limitation of the filtering and integration and differentiation procedure used was revealed when comparing results obtained at lower and higher levels of the tower. It was observed that a good fit of the processed results at the base level between DIC,

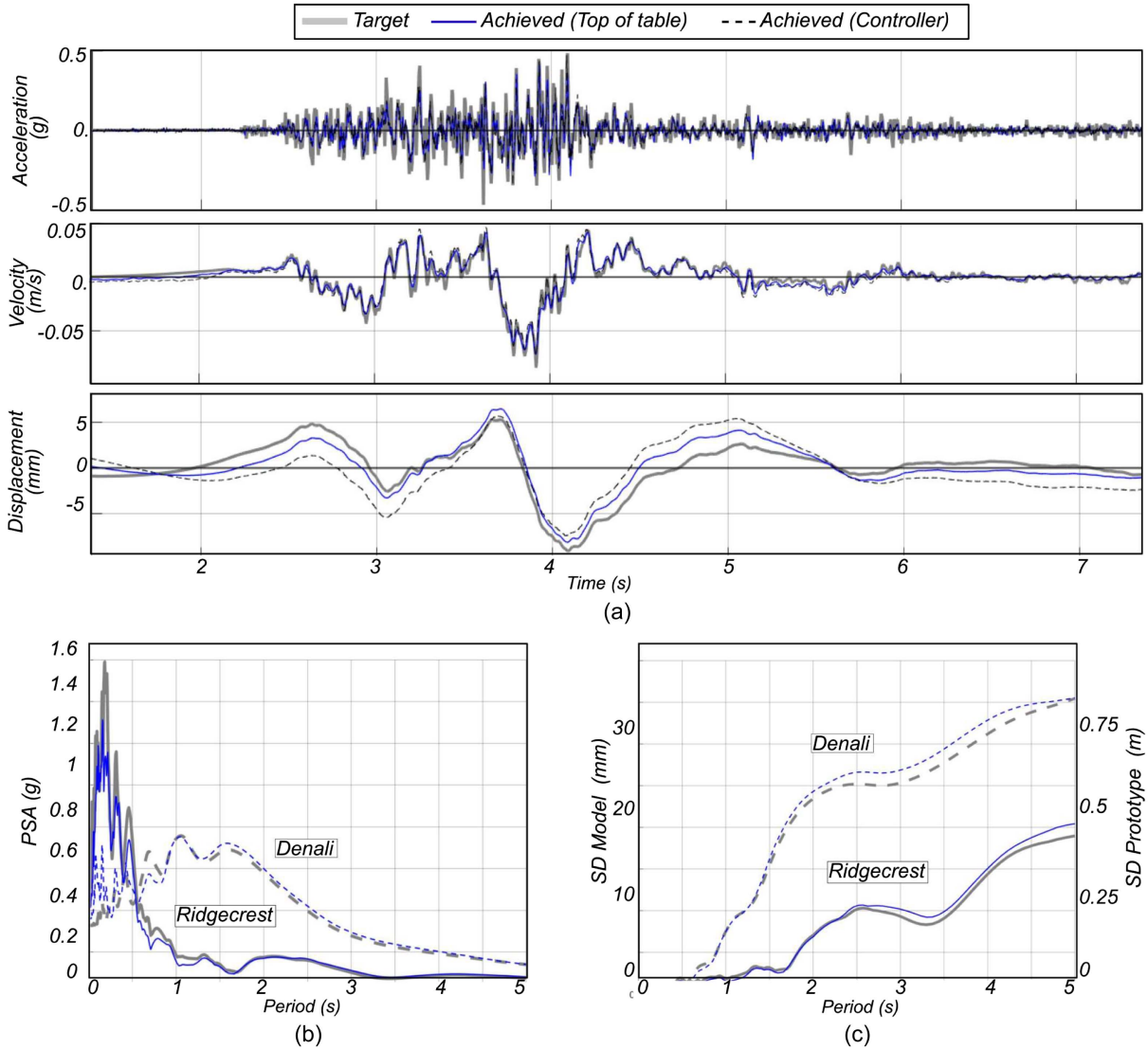

Fig. 13. Target versus achieved earthquake input ground motion: (a) time history of Tower 1 subjected to Ridgecrest 3-D, Run 1, x_1 direction; (b) acceleration; and (c) displacement response spectra from Ridgecrest 3-D, Run 1, and Denali 3-D x_1 direction.

accelerometers, and controller feedback did not necessarily imply that the filtering parameters used were the best option to process the raw measurement data at upper levels. As stated by Akkar and Boore (2009), tilting and rocking of accelerometers can induce long-period noise in the recorded acceleration. This causes a drift in the baseline of the record, leading to nonzero velocity at the end, which is nonphysical. Furthermore, these issues cause inaccuracies in the computed displacement responses. This effect can be observed in the absolute and relative displacement response time histories in Figs. 11 and 12. Closer to the base, there was a good agreement between the DIC data and the integrated displacement. However, at higher levels, where tilting and rocking were more prevalent, the discrepancies increased. Therefore, the peak displacement obtained from integration should not be considered definitive for describing the response of the MTS. In this case, DIC provided more reliable measured displacement results. Nonetheless, the computed displacement records are still useful for evaluating the overall response of the tower.

Tower 3 was tested three times with the same single-component input ground motion corresponding to the strong component of the 2019 Ridgecrest Earthquake recorded at the China Lake station. Some blocks exhibited visible residual displacement offsets during the first two tests, which eventually led to the tower's collapse shortly after the end of the third test. Fig. 14 shows the peak acceleration, velocity, and displacement response (i.e., response envelopes) along the height of the tower for each of the three tests. The solid and dashed lines represent the total and relative responses, respectively. The acceleration and velocity response envelopes for the three tests were similar, which agrees with the DIC time-history results presented in Fig. 7(b). This dynamic reproducibility was also observed for repeated tests at 1:107 scale (Rosakis et al. 2021). The relative displacement response envelope, on the other hand, which depends on the residual deformation of the tower from previous tests, shows an increase in the maximum relative displacement response from test to test, confirming the visual observations.

Unlike the full contour maps provided by DIC, accelerometers allowed us to evaluate the response time history only at the selected blocks along the spine of the tower. However, the locations of several sensors on a single block, as seen in Fig. 6(b), provided more localized information not captured by DIC. The information includes intrablock rotation, interblock rotation, and block sliding.

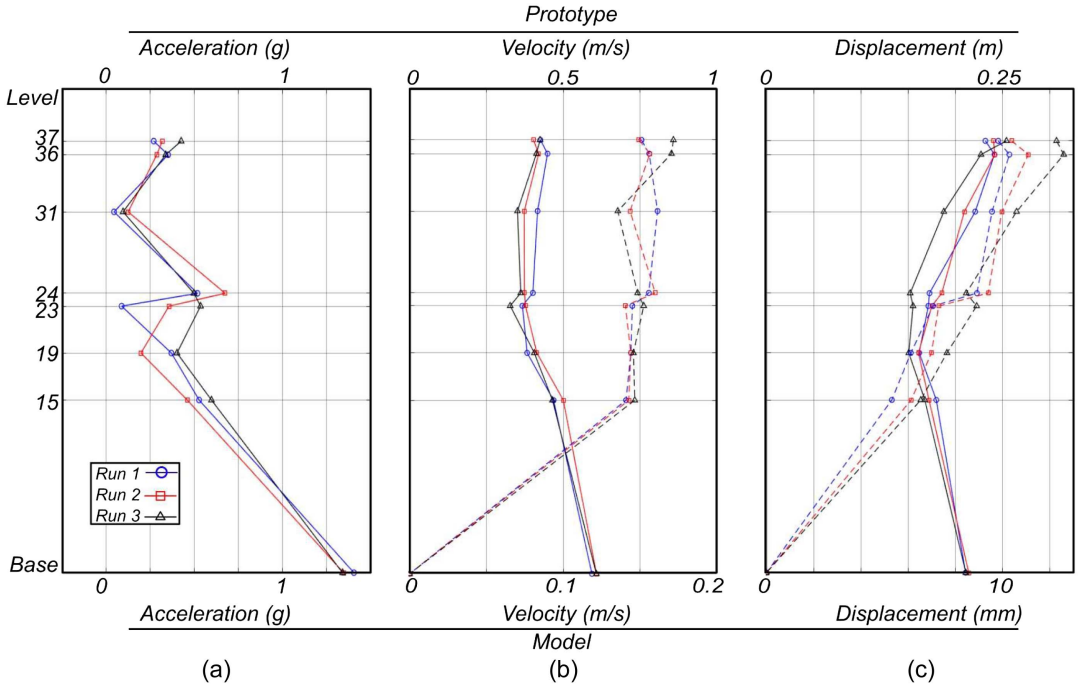

Fig. 14. Response envelope for Tower 3 subjected to Ridgecrest 1-D at model (tested specimen) and prototype (real-world tower) scales. Total response (solid) and relative response (dashed).

The time histories of these results are shown in Figs. 15 and 16. Rotation was computed using the difference between the top and bottom displacements of a single block assuming small rotations, $\tan(\theta) \approx \theta$. Once the intrablock rotation was computed, the rotation response was differentiated in the frequency domain to obtain the angular velocity and acceleration responses shown in Figs. 15(b and c).

Interblock rotation refers to the difference between the rotations (i.e., relative rotation) of two blocks at consecutive levels, that is, one on top of the other. Thus, this relative rotation could only be calculated at levels 36–37 and levels 23–24; see Fig. 16(a). Finally, block sliding was determined by taking the difference between the relative displacement responses of two blocks at consecutive levels. Block sliding displacement and velocity time histories are shown in Figs. 16(b and c), respectively.

Discussion of Test Results

This section discusses the key collapse mechanisms observed during the testing of Towers 1, 2, and 3, as well as the differences in the structural speed estimated from the test data. Additionally, key response quantities obtained using both DIC and accelerometers are compared for Towers 2 and 3. Finally, local interblock and intrablock responses derived from accelerometer measurements are discussed for Tower 3.

Collapse Mechanisms

The MTSs presented two distinct failure modes: (1) midheight buckling and (2) upper-block peeling. Towers 1 and 3 exhibited an upper block peeling collapse, whereas Tower 2 exhibited a buckling mode of collapse; see Figs. 8(a and b), respectively. These failure modes are consistent with the smaller-scale testing on the same ground motions (Rosakis et al. 2021). The collapse mechanisms could be observed in the accelerometer records. Due to the limitations of the filtering procedure previously explained and the difficulty of processing the data after the initiation of collapse had begun, unprocessed acceleration results were used to identify the onset of collapse. As previously mentioned, Fig. 9 indicates through dots the time instants at which collapse initiated along the height of the tower, and their sequence in time is congruent with the observed collapse mechanisms. Moreover, when the dots are connected, the dashed line follows the collapse profiles observed on the snapshots from Fig. 8, confirming the collapse behaviors observed during the experiments.

Structural Speed

Regarding the structural speed results, a difference as large as 10 m/s was observed when comparing the results obtained from DIC and the accelerometers. Differences in the recorded data due to the different locations of the sensors and the effects of the shake table motion in the x_2-direction and x_3-direction have already been discussed. However, the sensitivity of the structural speed is worth being analyzed. Given that time was scaled down by a factor of 5 (see Table 1), the time delay used when computing the structural speed was in the order of 1E-1. Thus, with a height of 6.46 m, small changes in the time delay caused larger differences in the computed structural speed. For example, for Tower 3-Run 3, the time delays from the DIC data and accelerometer data were found to be 0.089 and 0.104 s, respectively. The 0.015-s time delay difference between the two sensing methods caused a 16% variation in the structural speed.

Furthermore, results from both DIC and accelerometers from Towers 1 and 3 showed a decrease in structural speed after each repetition of the ground motion. The results suggest that the cumulative damage could have affected this magnitude. The dislocation of blocks from a previous run modified the initial condition of the specimen, thus affecting the structural speed. Blocks' height variability (which modifies the initial condition of the tower) and its effect on the structural speed was analyzed by Harmon et al. (2023).

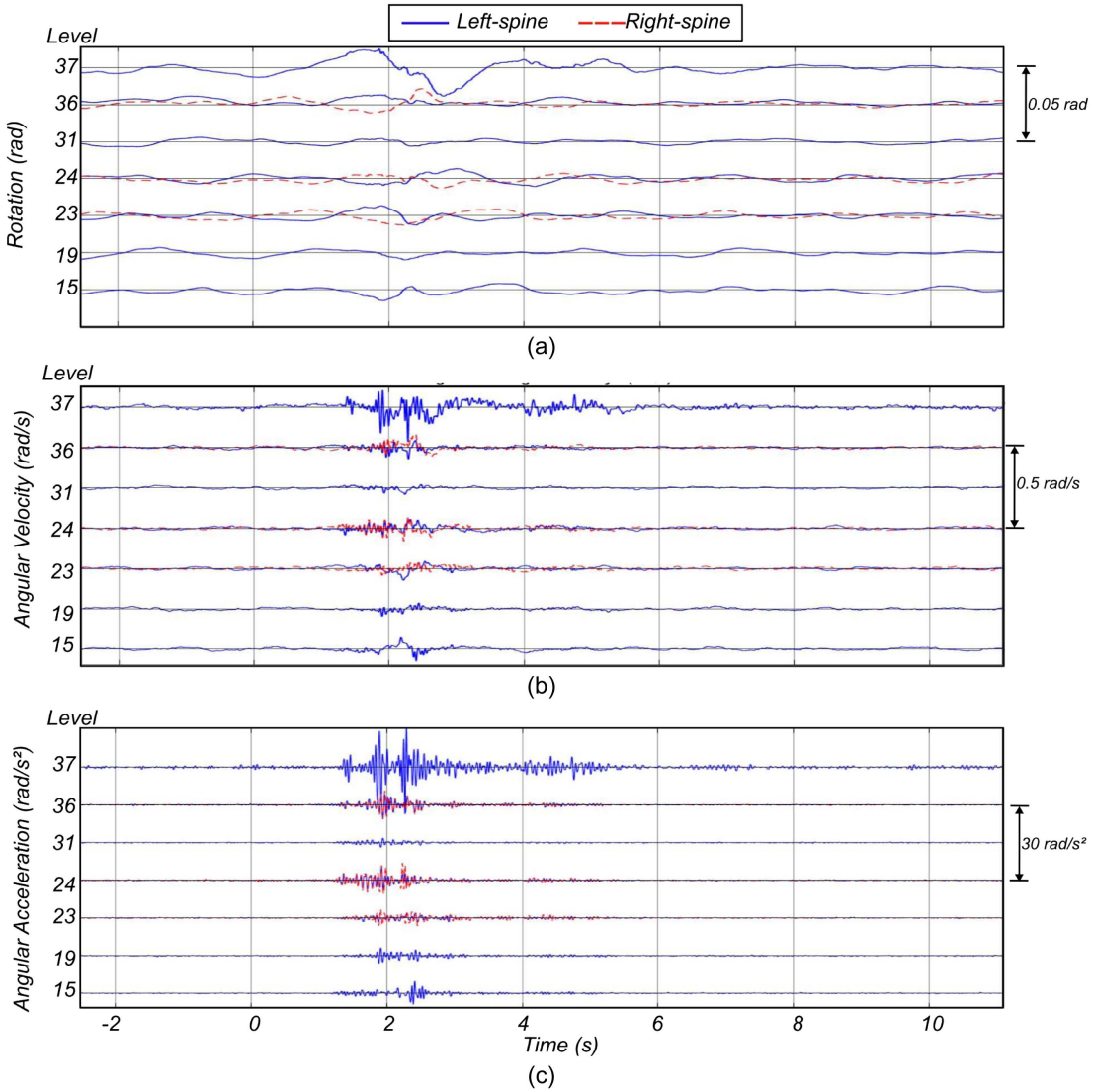

Fig. 15. Intrablock rotation response time-histories For Tower 3 subjected to Ridgecrest 1-D, Run 1: (a) block rotation; (b) angular velocity; and (c) angular acceleration responses.

However, further research in the topic will be necessary to better understand how the initial conditions of the specimen relate to the structural speed.

Key Response Quantities for Tower 2: Denali 3-D

A singular behavior worth discussing is the x_2-direction response of Tower 2 during the Denali 3-D input ground motion. Following the discussion of the structural speed illustrated in Fig. 10, it was observed that in the x_1-direction and x_3-direction, the total response along the height of the tower followed the response at the base. Furthermore, the slopes connecting the points of onset of sliding were similar throughout the height of the tower. However, this was not the case in the x_2-direction, as shown in Fig. 10(b). It is clearly seen that the blocks at level 15 and up did not follow the motion observed at base level. This response behavior suggests that the dislocations between the blocks in the x_2-direction were larger than the ones in the x_1-direction. This is an unexpected behavior given that the interlocking pattern [Figs. 1(b and c)] alternates its orientation along x_1 and x_2 at every level. Similar results were observed for Tower 3 subjected to Ridgecrest 1-D when analyzing the out-of-plane motion (in the x_2-direction). Furthermore, data output from DIC did not capture the out-of-plane response; thus, results obtained from accelerometer data results could not be compared to DIC in this case.

Key Response Quantities for Tower 3: Ridgecrest 1-D

An important aspect of Tower 3 is that it was tested three times sequentially. In Fig. 14, it is observed that the acceleration and velocity (both total and relative) response envelopes are very similar for the three runs. This was corroborated by comparing the entire response time histories. Nonetheless, when looking at the displacement response envelopes, it is evident that the maximum relative displacement, accounting for residual displacements from the previous tests, increased after each run. From these results, it was observed that the only differences in the tower configuration before each of the three tests or runs were the initial imperfections (i.e., previous residual displacements), which eventually led to collapse of the tower.

Residual displacement was computed by taking an average of the displacement values toward the end of the relative displacement

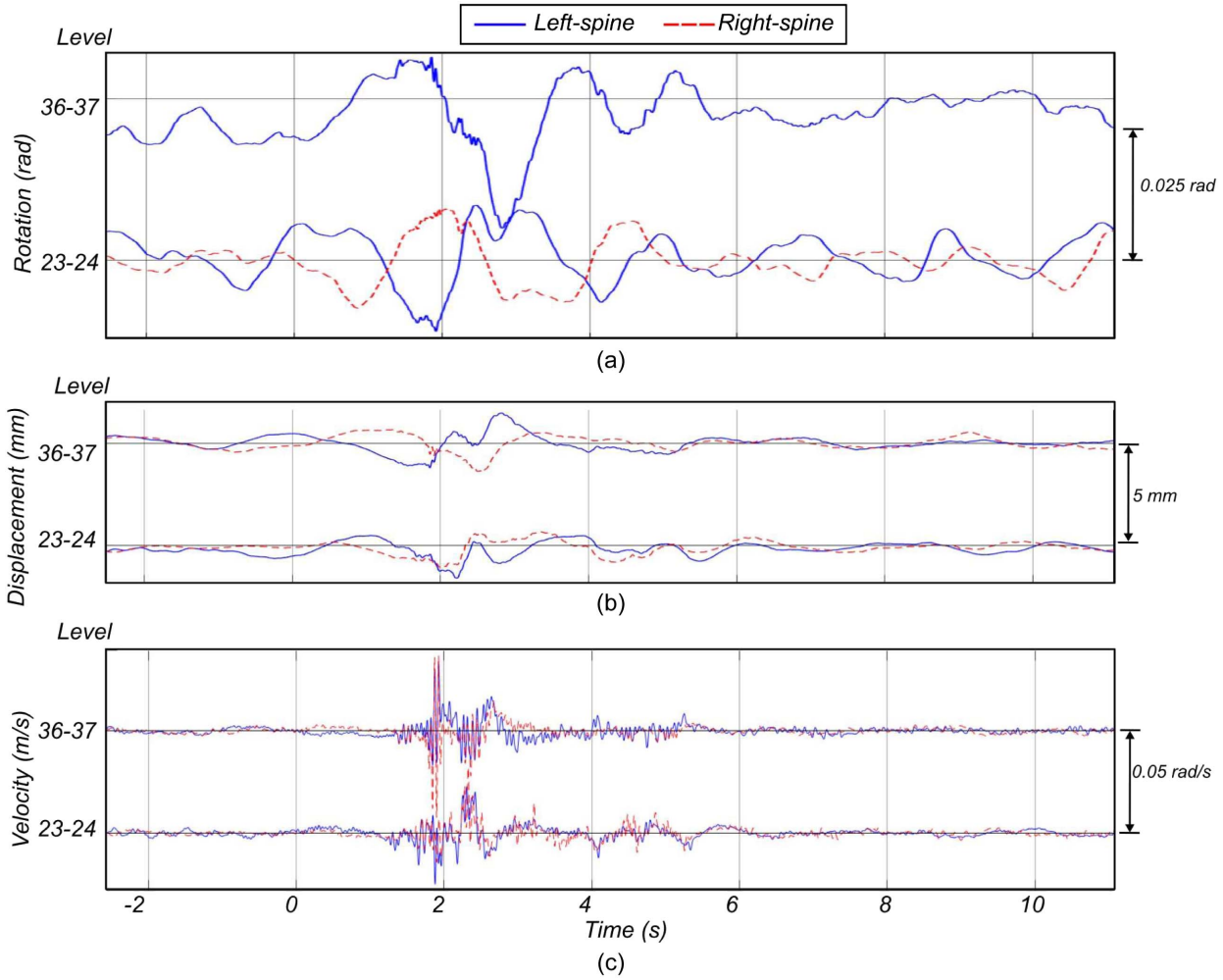

Fig. 16. Interblock response time-histories for Tower 3 subjected to Ridgecrest 1-D, Run 1: (a) interblock rotation; (b) interblock displacement/sliding; and (c) interblock velocity response.

record. As explained earlier, the displacement records are very sensitive to the filtering parameters applied before integration. Therefore, the residual displacement values obtained did not allow an accurate prediction of the exact residual displacements expected at other scales. The objective of computing these quantities was to account for the existing deformation of the tower from a previous run of the test.

Another aspect worth discussing is the similarity between the particle velocity derived from DIC and the accelerometer data. Velocity was used as the ground for comparison because the DIC particle velocity was computed through numerical differentiation of the measured particle displacement, whereas the accelerometer particle velocity was obtained through integration of the measured acceleration. The good fit of the results in Fig. 11(a) provides confidence that the signal processing parameters were selected appropriately. Moreover, the DIC displacement results served as a reference to check the doubly integrated acceleration data. As previously mentioned, long-period noise induced by rocking of the blocks influenced the filtering and integration procedures used to obtain the displacement response. This can be observed in Figs. 11(b) and 12(b) as an offset between the DIC and accelerometer-based results. Nonetheless, the good agreement is still surprising, considering that the data were recorded on opposite sides of the tower specimen. Therefore, the setting and calibration of the filtering parameters using two fundamentally different measurement systems proved successful, despite the limitations encountered.

As previously mentioned, it was observed that the front and back of the tower behaved very similarly during the seismic base excitations. This was observed not only during the Ridgecrest 1-D tests but also during the Denali 3-D test at lower levels. This behavior suggests that the block arrangement pattern at each level, as seen in Figs. 1(b and c), provided an adequate interlocking mechanism between blocks throughout the entire tower.

Additional information was obtained from the individual block results shown in Figs. 15 and 16. First, it is clearly seen that adjacent blocks were rotating out of phase. This suggests that some blocks were rocking independently during the seismic response. However, the magnitude of the rotations was small, and despite the blocks tilting independently, the full tower behaved as an interconnected structure. Moreover, isolated large peaks were observed when analyzing the intrablock and interblock rotation in Figs. 15(a) and 16(a), respectively. These peaks are even more evident in the rotational acceleration response shown in Fig. 15(c). This observation suggests that adjacent blocks were clashing into each other while rotating, meaning that the blocks interacted not only with the blocks immediately above and below but also with the horizontally adjacent blocks. These impacts between blocks in both the horizontal and vertical direction, although induced by very small rotations, contributed to the energy dissipation capacity of the structure that

allowed the tower to withstand two consecutive tests before collapsing shortly after the end of the third one.

Conclusions

Three model MTS towers were successfully built at a 1:25 scale and tested until collapse under one-component and three-component strong earthquake ground motions. The towers were composed of unbonded concrete blocks representing a gravity energy storage system. The construction of each tower involved a multiday procedure that required a construction crew and a carefully designed assembly system to minimize the geometric imperfections when building the specimen. However, despite the quality control measures, small imperfections were still observed in each of the three constructed towers. Experimental results allowed analysis of the seismic response of the structure beginning with the propagation of the seismic wave until collapse. Moreover, the seismic shake table tests provided important data for numerical model calibration and comparison across the scales 1:107 and 1:25, for which the μ number proved very effective for scaling purposes.

The motion of all particles in the front of the tower was successfully captured with DIC, whereas accelerometers measured the particle motions at the back of the tower. Despite the imperfections of the specimen and the location of the accelerometers on the opposite side of the tower, both measurement methods provided processed results that closely resembled each other.

Accumulation of damage was observed on two towers, which were able to withstand two subsequent repetitions of the same input ground motion before collapsing after the third. The vibrational response during each subsequent test was very similar to the prior test with the exception of the accumulated residual displacement field, which led to the collapse of the tower. On the other hand, the tower subjected to the near-fault Denali Earthquake ground motion collapsed during the first execution of the test. Furthermore, two distinct modes of failure were identified. An upper-block peeling failure was observed on the towers subjected to the three subsequent ground motions, whereas the tower subjected to the near-fault ground motion exhibited a midheight buckling collapse mechanism. These observed failure modes were corroborated with the data captured by the accelerometers.

The block velocity response was used to evaluate the arrival of the first seismic wave at every level of the tower along the spine. The velocity at which the motion propagated from the base to the top of the tower was defined as the structural speed. Furthermore, the propagation of the wave along the height of the tower that the tower responded as an interconnected structure despite the absence of any bonding material between the blocks. Moreover, both DIC and accelerometers provided consistent (similar) structural speed values that could also be scaled using the μ number.

Finally, accelerometers were effective at determining the response of single (vertically and horizontally) adjacent blocks. With results from the interblock and intrablock rotations and block sliding, it was possible to identify relative rotations of neighboring blocks and impacts between them. The block rocking and impact response mechanism, along with the friction involved in block sliding, both reproduced analytically In Harmon et al. (2023), contributed to the energy dissipation capacity of the MTS towers.

Data Availability Statement

All data, models, or code that support the findings of this study are available from the corresponding author upon reasonable request.

Acknowledgments

We gratefully acknowledge the support, encouragement, and freedom provided by Energy Vault, Inc. during this project. We also thank the contractors (Whiteside Concrete Construction, Dynamic Isolation Systems, BlockMex, Luka Grip and Lighting, Abel-Cine, Samy's Camera) and university facility personnel at UC Berkeley for their commitment to this project.

Supplemental Materials

Videos S1–S4 are available online in the ASCE Library (www.ascelibrary.org).

References

Adafruit. 2021. "Analog devices ADXL335–5V ready triple-axis accelerometer (+–3g analog out)." Accessed 7 July, 2022. https://www.adafruit.com/product/163.

Akkar, S., and D. Boore. 2009. "On baseline corrections and uncertainty in response spectra for baseline variations commonly encountered in digital accelerograph records." *Bull. Seismol. Soc. Am.* 99 (3): 1671–1690. https://doi.org/10.1785/0120080206.

Andrade, J., A. Rosakis, J. Conte, J. Restrepo, V. Gabuchian, J. Harmon, A. Rodriguez, A. Nema, and A. Pedretti. 2023. "A framework to assess the seismic performance of multiblock tower structures as gravity energy storage systems." *J. Eng. Mech.* 149 (1): 04022085. https://doi.org/10.1061/(ASCE)EM.1943-7889.0002159.

ARRI. 2023. "ARRI lightinig." Accessed February 16, 2024. https://www.arri.com/en/lighting/tungsten.

Baldi, J., and V. Roux. 2016. "The innovation of the potter's wheel: A comparative perspective between Mesopotamia and the southern levant." *Levant* 48 (3): 236–253. https://doi.org/10.1080/00758914.2016.1230379.

Barnhart, W. D., G. P. Hyes, and R. D. Gold. 2019. "The July 2019 Ridgecrest, California, earthquake sequence: Kinematics of slip and stressing in cross-fault ruptures." *Geophys. Res.* 46 (11): 859–867. https://doi.org/10.1029/2019GL084741.

BP (British Petroleum). 2022. "BP statistical review of world energy 71st ed." Accessed February 17, 2023. https://www.bp.com/content/dam/bp/business-sites/en/global/corporate/pdfs/energy-economics/statistical-review/bp-stats-review-2022-full-report.pdf.

Correlated Solutions. 2022. "Vic-2D digital image correlation." Accessed February 17, 2023. https://www.correlatedsolutions.com/vic-2d.

Dunham, E., and R. Archuleta. 2004. "Evidence for a supershear transient during the 2002 Denali fault earthquake." *Bull. Seismol. Soc. Am.* 94 (6B): S256–S268. https://doi.org/10.1785/0120040616.

EIA (US Energy Information Administration). 2021. "International energy outlook 2021." Accessed February 3, 2023. https://www.eia.gov/outlooks/ieo/consumption/sub-topic-03.php.

Harmon, J., V. Gabuchian, A. Rosakis, J. Conte, J. Restrepo, A. Rodriguez, A. Nema, A. Pedretti, and J. Andrade. 2023. "Predicting the seismic performance of multiblock tower structures using level set discrete element method." *Earthquake Eng. Struct. Dyn.* 52 (9): 2577–2596. https://doi.org/10.1002/eqe.3883.

Harris, H., and G. Sabnis. 1999. *Structural modeling and experimental techniques*. 2nd ed. Boca Raton, FL: Taylor and Francis.

McLarnon, F., and E. Cairns. 1989. "Energy storage." *Ann. Rev. Energy* 14 (1): 241–271. https://doi.org/10.1146/annurev.eg.14.110189.001325.

Moncarz, P., and H. Krawinkler. 1981. *Theory and application of experimental model analysis in earthquake engineering*. Rep. No. 50. Stanford, CA: Stanford Univ.

Pennock, G. 2007. "James Watt (1736–1819)." In *Distinguished figures in mechanism and machine science: Their contributions and legacies part 1*, edited by M. Ceccarelli, 1st ed., 337–369. Dordrecht, Netherlands: Springer.

Phantom. 2023. "4K and media production." Accessed February 16, 2024. https://www.phantomhighspeed.com/products/cameras/4kmedia.
Piccolino, M. 2000. "The bicentennial of the voltaic battery (1800–2000): The artificial electric organ." *Trends Neurosci.* 23 (4): 147–151. https://doi.org/10.1016/S0166-2236(99)01544-1.
Quijada-Publins, R. 2021. "Mapping the history of sailing." *Water History* 13 (3): 427–471. https://doi.org/10.1007/s12685-021-00292-6.
Rao, J. 2011. Vol. 20 of *History of rotating machinery dynamics*. New York: Springer.
Rosakis, A., J. Andrade, J. Conte, J. Restrepo, V. Gabuchian, J. Harmon, A. Rodriguez, A. Nema, and A. Pedretti. 2021. "Implications of Buckingham's pi theorem to the study of similitude in discrete structures: Introduction of the RNF, μN, and SN dimensionless numbers and the concept of structural speed." *J. Appl. Mech.* 88 (9): 091008. https://doi.org/10.1115/1.4051338.
Schoneich, S. 2014. "From global decisions and local changes. The ceremonial dance of the Voladores becomes UNESCO intangible cultural heritage." *Ethnologies* 36 (1–2): 447–466. https://doi.org/10.7202/1037617ar.
TEC (TE Connectivity). 2023. "Measurement specialty sensors (MEAS) products." Accessed June 19, 2023. https://www.te.com/usa-en/products/brands/meas.html?tab=pgp-story.
UCB (University of California Berkeley). 2023. "UC Berkeley simulator laboratory." Accessed June 19, 2023. https://peer.berkeley.edu/uc-berkeley-simulator-laboratory.
UN (United Nations). 2021. "The Paris agreement." Accessed February 2, 2023. https://www.un.org/en/climatechange/paris-agreement.
UNWH (United States White House). 2021. "The long term strategy of the United States: Pathways to net-zero greenhouse gas emissions by 2050." Accessed June 15, 2023. https://www.whitehouse.gov/wp-content/uploads/2021/10/US-Long-Term-Strategy.pdf.
USDE (United States Department of Energy). 2023. "The pathway to long duration energy storage commercial liftoff." Accessed June 15, 2023. https://liftoff.energy.gov/long-duration-energy-storage/.